Journal of Thermal Analysis and Calorimetry (2023) 148:3035–3044
https://doi.org/10.1007/s10973-022-11472-8

Thermofluid behaviour of boron nitride nanotube nanofluid in a microchannel under optimized conditions

Mohamad Nur Hidayat Mat[1] · Normah Mohd-Ghazali[1] · Hielfarith Suffri Shamsuddin[1] · Patrice Estellé[2]

Received: 18 November 2021 / Accepted: 21 June 2022 / Published online: 26 July 2022
© Akadémiai Kiadó, Budapest, Hungary 2022

Abstract
While numerical modelling of different types of nanofluids in various microchannel heat sink geometry under different flow conditions are many, few involved utilizations of experimental data. Reports so far have indicated the potential cooling capability of nanofluids in general, yet none have investigated the effects of the surfactant alone on the fluid flow, in particular the thermofluid flow pattern. This paper reports the results of a numerical simulation with CFD on the fluid flow of Triton TX-100 surfactant with boron nitride nanotubes (BNN) in distilled water (base fluid) at 30 and 50 °C. The nanofluid (BNNT) operated at high temperature provided a lower thermal resistance. A higher pumping power was found for BNNTs and TX-100 at 30 ℃ compared to distilled water at both temperatures. The outcomes of the present study provide a better understanding of flow characteristic and flow visualization along a microchannel heat sink so that better design decision can be made for improvement of this application for different needs.

Keywords Numerical simulation · Boron nitride nanotubes · Surfactant · Microchannel

Introduction

Microchannel heat sink (MCHS) is a micron-sized heat exchanger that removes heat from electrical and electronic devices components to a cooling fluid medium. The conventional cooling medium is air or water due to their availability. Due to advanced development into the fourth industrialization revolution (Industry 4.0), heat flux from these devices is expected to increase exponentially, nanofluid coolant being at the forefront to replace air and water. Nanosized particles dispersed in a base fluid has been reported to increase the fluid's heat removal capability through the increase in the fluid's thermal conductivity. However, the nanofluid requires the presence of an additive, a surfactant, to prevent the nanoparticles from agglomeration and consequently clogging the channel [1]. Those surfactants stabilize nanoparticles by reducing interfacial tension between fluid and nanoparticles.

Many studies have been reported on the performance of the nanofluid as a coolant in general, at various concentrations, under various channel geometry. Most of the reports, however, involved modelling with hardly any utilizing experimental data. Investigations into the effects of the presence of the surfactant are also few due to the absence of data on the thermophysical properties of the base fluid, the surfactant and base fluid, and the final nanofluid mixture. A most recent paper by Shamsuddin et al. [2] reported the effects of the surfactant TX-100 on distilled water, the base fluid. The improvement in the thermal performance of the boron nitride nanotube (BNNT) nanofluid at 30 °C was attributed to the surfactant and not the BNNT. This paper reports the results of a numerical simulation with CFD on the fluid flow of Triton TX-100 surfactant and BNNT nanofluid, utilizing the same experimental data as that of Shamsuddin et al. [2].

Triton X-100 ($C_{36}H_{62}O_{11}$) is one of the most widely used non-ionic biodegradable detergents which is also being utilized as a surfactant to stabilize a nanofluid. An experimental study on a thermosyphon heat pipe application using TX-100 as surfactant reported that mixing nanofluid with TX-100 decreased the thermal resistance and increased the thermal efficiency of the heat pipe system [3]. Heat pipe efficiency can be increased up to 20.9% by adding approximately

✉ Mohamad Nur Hidayat Mat
mn.hidayat@utm.my

[1] School of Mechanical Engineering, Faculty of Engineering, Universiti Teknologi Malaysia, 81310 UTM Johor Bahru, Malaysia

[2] Univ Rennes, LGCGM, 35000 Rennes, France

around 2% of TX-100's concentration. The application of TX-100 has also been reported for use in a solar collector. The report stated that adding TX-100 to TiO_2 in nanofluid provided a better performance than pure water alone [4, 5]. In addition to this, Triton TX-100 strongly influenced the suspension stability and absorption characteristic of sunlight for multi-walled carbon nanotubes in nanofluid for the enhancement of solar thermal absorption [6–8]. The results reported by Shamsuddin et al. [2] indicated that further analysis of the effects of surfactant TX-100 on the base fluid BNNT is needed. To the best of our knowledge, no work has been reported on the characterization effect of surfactant TX-100 on BNNT nanofluid for MCHS's cooling enhancement using a CFD simulation approach.

In this study, a CFD simulation was conducted to investigate the thermofluid effects of heat transfer fluids in MCHS. This approach can clarify the flow and heat transfer patterns inside a MCHS with much more detail but rather reduced cost. Three different fluids were investigated based on the available experimental data of the thermophysical properties: distilled water alone, TX-100 in distilled water, and distilled water with TX-100 and BNNT. These three fluids were simulated at two different temperatures which were 30 and 50 °C, respectively. The results may better explain the outcomes reported by Shamsuddin et al. [2] on the increased/decreased thermal resistance and pressured drop of the three fluids at the temperatures investigated. Finally, this study may contribute to the understanding surfactant behaviour with nanofluid specifically for heat exchanger application.

System modelling

The three different fluid types investigated are listed in Table 1 with their fluid properties given in Table 2. Since the model employed numerical analysis, this analysis began with a 3D geometry creation using computer-aided design (CAD) to represent the computational domain. The dimensions of the microchannel are $10 \times 10 \times 0.213$ mm (length, L × width, W × substrate, t) as shown in Fig. 1.

The material of the MCHS is silicon. This analysis only considered a single symmetrical channel as proposed by

Table 1 Fluids investigated [2]

Fluid	Definition
Distilled water	No additives
TX-100 mix or base fluid	Distilled Water (H_2O) with 0.35 vol% of surfactant TX-100
BNNTs nanofluid 0.001 mass%	Distilled Water (H_2O) with 0.35 vol% of surfactant TX-100 and 0.001 mass% of Boron Nitride Nanotubes

Table 2 Fluid properties obtained from [9]

Condition of fluid	k/W m^{-1} K^{-1}	ρ/kg m^{-3}	C_p /kJ kg^{-1} K^{-1}	μ/Ns m^{-2}
Distilled water at 30 °C	0.536	997.0	4.017	0.756
TX-100 mix or base fluid at 30 °C	0.543	997.1	4.065	0.809
BNNTs nanofluid 0.001 mass% at 30 °C	0.544	997.4	4.076	0.808
Distilled water at 50 °C	0.560	989.8	4.004	0.505
TX-100 mix or base fluid at 50 °C	0.558	989.9	4.020	0.483
BNNTs nanofluid 0.001 mass% at 50 °C	0.567	990.2	4.115	0.494

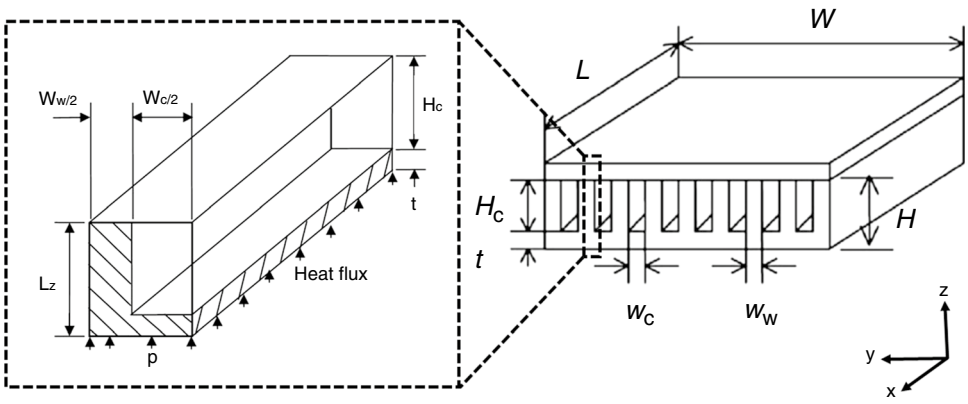

Fig. 1 Schematic drawing of MCHS model for computational domain

Husain and Kim [6] easing the computational load, and the convergence criteria for all residuals must be below 1 × 10–4 in order to obtain consistent numerical result. The validation process was conducted using the channel aspect ratio, α, and wall width ratio, β,

$$\alpha = \frac{H_c}{W_c}. \tag{1}$$

$$\beta = \frac{W_w}{W_c} \tag{2}$$

The design variables are listed in Table 3. Upon successfully obtaining the optimum grid resolution, CFD analysis proceeded with the optimum α and β so that this analysis can be compared with that by Shamsuddin et al. [2].

The mesh size selection was selected according to Guideline 14 of the American Society of Heating, Refrigeration and Air-Conditioning Engineers (AHSRAE). This guideline suggested the coefficient of variation for root-mean-square error, *CV(RSME)* lower than 15% and the statistical index, R^2, more than 0.95, where

$$\mathrm{CV(RMSE)} = \frac{\sqrt{\sum_{i=1}^{N_i}\left[\left[\left(M_i - S_i\right)^2\right]/N_i\right]}}{\left(1/N_i\right)\sum_{i=1}^{N_i} M_i} \tag{3}$$

which includes M_i the real value, S_i the predicted value, and N_i the total amount of data.

$$R^2 = 1 - \frac{\sum_i \left(M_i - S_i\right)^2}{\sum_i \left(M_i - \overline{M_i}\right)^2} \tag{4}$$

where $\overline{M_i}$ is the mean value of M_i. Heat transfer performance relates to the thermal resistance and pumping power to drive the coolant through the microchannel. The total thermal resistance is defined as:

Table 3 Design variables and constraints

Design variables	Value
α(reference)	5.218
β(reference)	1.0
α(optimum)	5.729
β (optimum)	0.413
Heat sink width, W (cm)	1.0
Heat sink length, L (cm)	1.0
Substrate thickness, t (cm)	0.0213
Channel height, H_c (cm)	0.032

$$R_{th} = \frac{\Delta T_{max}}{qA_s} \tag{5}$$

where q is defined as heat flux, A_s is substratum area, and ΔT_{max} is the maximum heat sink temperature rise defined as:

$$\Delta T_{max} = T_{s,o} - T_{f,i} \tag{6}$$

The pumping power required to drive the fluid through the sink can be evaluated with

$$\overline{P} = n \cdot u_{avg} \cdot A_c \cdot \Delta p \tag{7}$$

The pressure drop is represented by Δp, while n is the number of channels, A_c is a cross-sectional area of the channel that is perpendicular to fluid flow direction, and u denotes the average velocity for the fluid flow in the microchannel. There are five dimensionless numbers that are pertinent to the thermofluid analysis in the microchannel, the first is the Reynolds number,

$$Re = \frac{\rho u L}{\mu} \tag{8}$$

which represents the inertial force to viscous force. ρ is density, L is the channel path, and μ is dynamic viscosity. Next is the Brinkman number,

$$Br = \frac{\mu u^2}{k\left(T_w - T_f\right)} \tag{9}$$

which relates the heat conduction from a wall to a flowing viscous fluid. k is thermal conductivity, T_w is wall temperature, and T_f is fluid temperature. The Euler number expressed the relationship between a local pressure drop caused by a restriction and the kinetic energy per volume of flow,

$$Eu = \frac{p_u - p_d}{\rho u^2} \tag{10}$$

where p_u and p each is the upstream pressure and downstream pressure, respectively. The Nusselt number is the ratio of convective to conductive heat transfer across a boundary,

$$Nu = \frac{hL}{k} \tag{11}$$

with h being the local heat convection. Then, there the Prandtl number and Bejan number are defined as:

$$Pr = \frac{C_p.\mu}{k} \tag{12}$$

$$Be = \frac{\Delta p L^2}{\mu u_{avg}} \tag{13}$$

where *C*p is a local specific heat of fluid.

$$f = \frac{\Delta pL}{\frac{1}{2}Lu_{\text{avg}}^2} \tag{14}$$

f is friction factor along a channel path, L. This simulation involved flow and heat transfer processes at steady state, incompressible Newtonian fluid flow with no external force. The governing equations are required for the computational domain: mass, momentum, and energy conservation [10] for convection in the microchannel. These are expressed in tensor forms as follows:

Conservation of mass:

$$\frac{\partial \rho_{\text{f}}}{\partial t} + \frac{\partial \rho_{\text{f}} u_{\text{i}}}{\partial x_{\text{i}}} = 0 \tag{15}$$

Conservation of momentum:

$$\rho_{\text{f}} \frac{\partial u_{\text{i}}}{\partial t} + \rho_{\text{f}} \frac{\partial u_{\text{i}}}{\partial x_{\text{j}}} = -\frac{\partial p}{\partial x_{\text{i}}} + \rho_{\text{f}} g_{\text{i}} + \frac{\partial}{\partial x_{\text{j}}}\left(\mu_{\text{f}} \frac{\partial u_{\text{i}}}{\partial x_{\text{j}}}\right) + \frac{\partial}{\partial x_{\text{j}}}\left(\mu_{\text{f}} \frac{\partial u_{\text{j}}}{\partial x_{\text{ii}}}\right) - \frac{2}{3}\frac{\partial}{\partial x_{\text{j}}}\left(\mu_{f} \frac{\partial u_{\text{k}}}{\partial x_{\text{k}}}\right) = 0 \tag{16}$$

Conservation of energy:

$$\rho_{\text{f}} \frac{\partial h}{\partial t} + \rho_{\text{f}} u_{\text{j}} \frac{\partial h}{\partial x_{\text{i}}} = \frac{\partial p}{\partial t} + u_{\text{i}} \frac{\partial p}{\partial x_{\text{i}}} + \frac{\partial}{\partial x_{\text{i}}}\left(k_{\text{f}} \frac{\partial T_{\text{f}}}{\partial x_{\text{i}}}\right) + \tau_{\text{ij}} \frac{\partial u_{\text{i}}}{\partial x_{\text{j}}} (\text{Fluid domain}) \tag{17}$$

$$\frac{\partial}{\partial x_{\text{i}}}\left(k_{\text{s}} \frac{\partial T_{\text{s}}}{\partial x_{\text{i}}}\right) = 0 (\text{Substrate conduction}) \tag{18}$$

The mathematical formulation requires solving the boundary conditions repeatedly in each cell centroid as given in Table 4. A continuous homogeneous heat flux, q, of 790 W cm^{-2} was set as the boundary condition at the bottom wall of the heat sink. By contrast, most of the outside walls were believed to be completely insulated from the environment. The x and y coordinates of the heat sink planes are subjected to symmetrical boundary requirements. The volume flow rate and temperature of the fluid entering the heat sink inlets were set at 4.7 cm^3 s^{-1} and 30 °C, respectively, while the channel outlet had a constant static pressure barrier condition. Temperature and heat flow continuity acted as the conjugate boundary condition connecting the fluid and wall energy equations. Equations (15)–(18) were numerically solved using a finite volume CFD solver Ansys Fluent 2020 R2.

Results and discussions

Refinement of the computational mesh was applied between the solid and fluid layers with a growth rate of 1.2 and a minimum of 0.005 mm. This refinement was needed to resolve the viscous shear layer correctly and capture the conjugate boundary conditions. After the mesh was successfully established, grid independent test was conducted to provide the highest mesh accuracy [15–19]. In this current test, eight different meshes were created which was represented by the grid resolution. This resolution started with 4 to 32 with an increment of 4 as shown in Table 5. The pressure drop and thermal resistance were the point of interest. Based on the generated results, grid resolution 28 was chosen for this study because it satisfied that the criteria of R^2 should be more than 0.95 and CV(RSME) less than 15%. Overall,

Table 4 Setup of CFD boundary conditions

Boundary condition	Value	Source
Analysis type	Steady state	Hong et al. [11]
Type of flow	Laminar	Hong et al. [11]
Number of cycles	400	Minimum iteration for convergence
Ambient and inflow temperature	30 °C	Hong et al. [11]
Inlet flux	4.7 cm^3 s^{-1}	Halelfadl et al. [12]
Outlet flux	0 Pa	Static pressure (outflow)
Heat flux	790 W cm^{-2}	Tuckerman, Pease [13]
Pressure correction type	SIMPLE method	Hong et al. [11]
Mass convergence criteria	1×10^4	Husain, Kim [14]
Velocity convergence criteria	1×10^4	Husain, Kim [14]
Energy convergence criteria	1×10^7	Husain, Kim [14]

Table 5 Grid independence test

Grid resolution	Simulated pressure drops (P)	Simulated thermal resistance (R)	CV(RSME) of P	CV(RSME) of R	R^2 of P	R^2 of R
32	15.45	0.11	3.35	1.63	1.00	1.00
28	14.23	0.11	5.74	9.45	0.99	0.99
24	14.05	0.12	7.08	17.28	0.99	0.96
20	7.81	0.12	53.59	25.10	0.48	0.92
16	6.45	0.13	63.73	30.90	0.27	0.89
12	6.09	0.13	66.41	42.89	0.21	0.78
8	5.12	0.13	73.64	50.41	0.02	0.70
4	5.01	0.14	74.46	54.48	0.00	0.65

these comparisons clearly indicate promising numerical accuracy for further numerical analysis.

Flow characteristics along the relative length of a microchannel in the heat sink is shown in Fig. 2 where the values have been taken at $z/Hc = 0.5$ at the $y/wc = 0.5$. Figure 2a presents Re across the relative length for the three different fluids investigated, at 30 and 50 °C. Due to the lower density and much lower viscosity of the fluids at 50 °C (Table 2), the Re is 49–67% higher than that at 30 °C. The graph reveals that the Re begins to increase at a microchannel's entrance until reaching 0.2 of relative length for all the fluids at both temperatures. This indicates that the entrance length for all the fluids is around 0.2 cm. The average Re for distilled water, TX-100, and BNNTs at 50 °C is about 650, while the rest of the fluid operated at 30 °C around 400. Figure 2b shows the Brinkman number, Br, along the channel. The results show that initially the Br is low for all fluid types but increases along the MCHS length. Obviously, Br for TX-100 and BNNTs at 30 °C are the highest among other fluids, and higher heat transfer by viscous dissipation due to the higher viscosity at that temperature. The pressure drop along MCHS length is shown in Fig. 2c, and it decreases linearly with an increase in relative length for all coolant types. This finding highlighted that the presence of BNNT and TX-100 at 30 °C produced the maximum pressure drop compared to other fluids, the presence of surfactant and nanoparticles increasing the frictional losses. The results agree with those reported by Shamsuddin et al. [2]. Figure 2d highlights the fluid's temperature across the relative length of MCHS. The temperature of all fluids increased steadily with further increment in relative length. The highest temperature is shown for distilled water, TX-100, and BNNT nanofluid at 50 °C. The thermal resistance, Rth, along the channel length is shown in Fig. 2g. In the present study, the point of measurement located is specific which is at the middle section of the fluid flow ($z/Hc = 0.5$, $y/wc = 0.5$). Figure 2h presents the pumping power, P, across the MCHS's length. This naturally follows the pattern of the pressure drop at a fixed mass flow rate. Figure 2i highlights Bejan, Be, along the relative length. The Be decreased linearly with further increment in relative length. The maximum Be appeared to be TX-100 and BNNTs operating at 50 °C, while the lowest of Be was distilled water at 30 °C. The friction factor, f, along relative length of MCHS is shown in Fig. 2j. The f for all fluids decreases drastically along the relative length. This f relies heavily on pressure drop. The maximum *f* starts at inlet and decreases to the end of the length.

Clear visualization of complex flow can often help to understand better the fluid flows at various conditions. With CFD, stages of thermal and hydrodynamic developments in the fluid can easily be presented as shown in Figs. 3 through 6; the entrance region covers x/L from 0 to 0.2, while the exit covers x/L from 0.8 to 1. Figure 3 reveals the total pressure across the microchannel heat sink (MCHS) inlet and outlet in which the outlet pressure was setup at zero gauge pressure. The pressure drop is higher at 30 °C than at 50 °C, as observed earlier for the values presented at $z/H_c = 0.5$, in this case shown to be more homogenous across the plane in the former than in the latter for distilled water. Shamsuddin et al. [2] found that at 30 °C, the addition of surfactant TX-100 produced a significant change in both the thermal resistance and pressure drop of distilled water, while at 50 °C, any change observed was after the addition of BNNT nanoparticles. In terms of the flow visualization for temperature, Fig. 4 demonstrates the temperature for all fluids at the inlet and exit regions of the channel. Although the lower temperature (30 °C) fluids

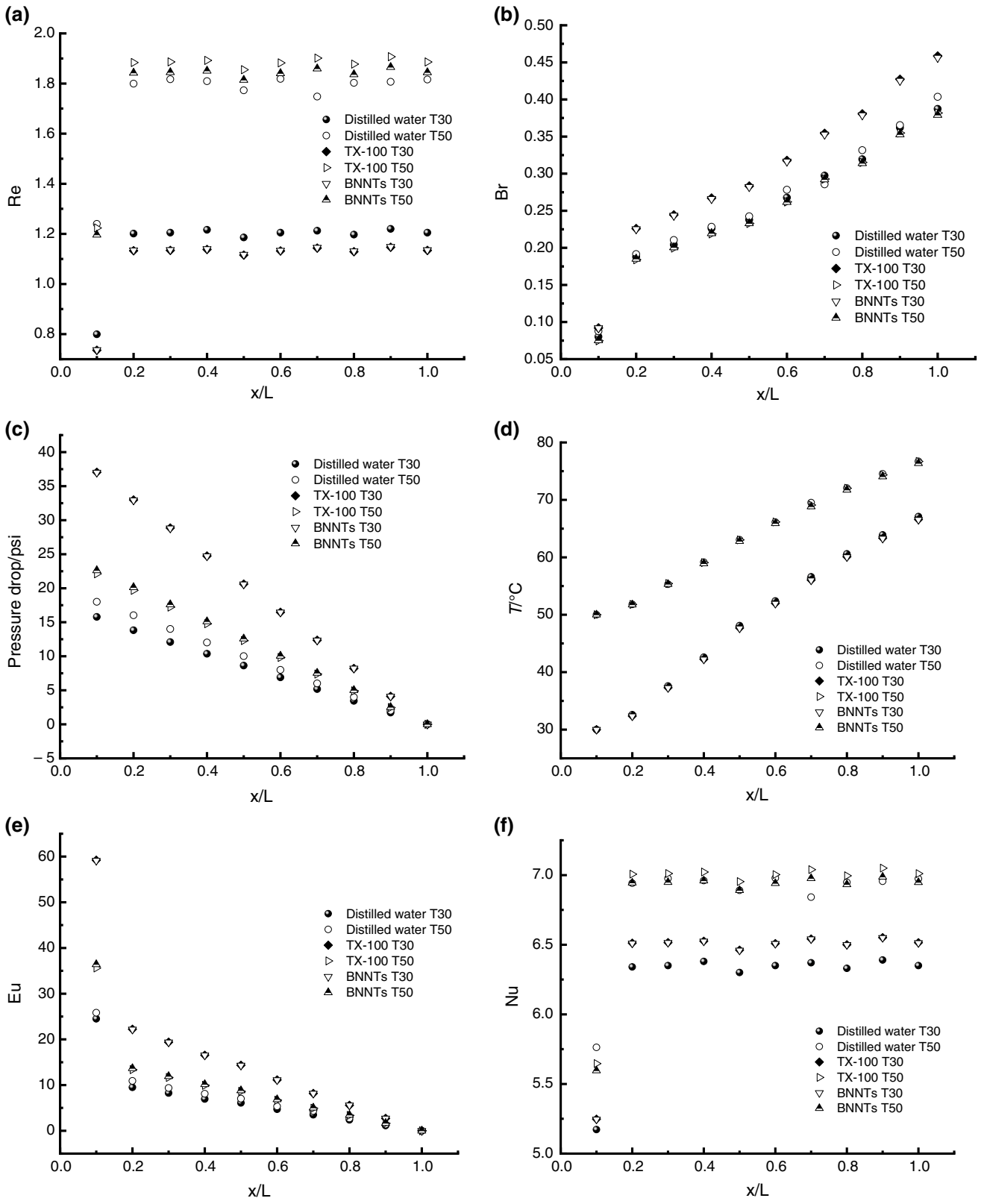

Fig. 2 Characteristic property along relative length

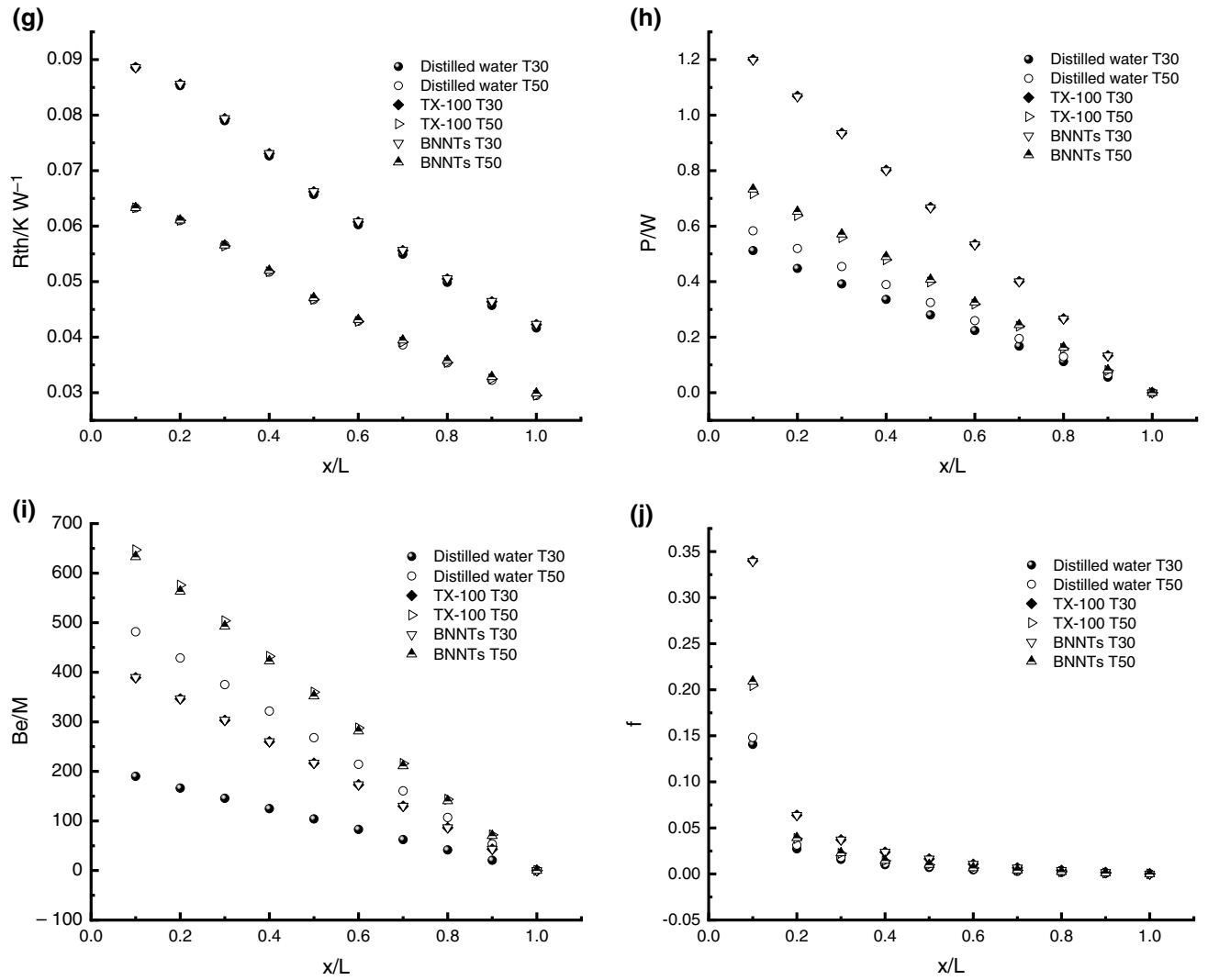

Fig. 2 (continued)

seem to have a higher temperature increase from the inlet to the exit region as shown in Fig. 2d, the fluids at 50 °C is more capable at absorbing the heat right at the entrance from the homogeneity of the temperature patterns. Since it is important to avoid hot spots along the microchannel to avoid thermal fatigue, operating at 50 °C is better than that at 30 °C. Figure 5 highlights the contour plot of velocity magnitude across MCHS length, and again the velocity patterns seem to be more homogenous in the 50 °C profiles for all the fluids investigated. Figure 6 shows the flow visualization in y-plane view for velocity, total pressure, and temperature at three relative lengths (x/L = 0.1, 0.5,

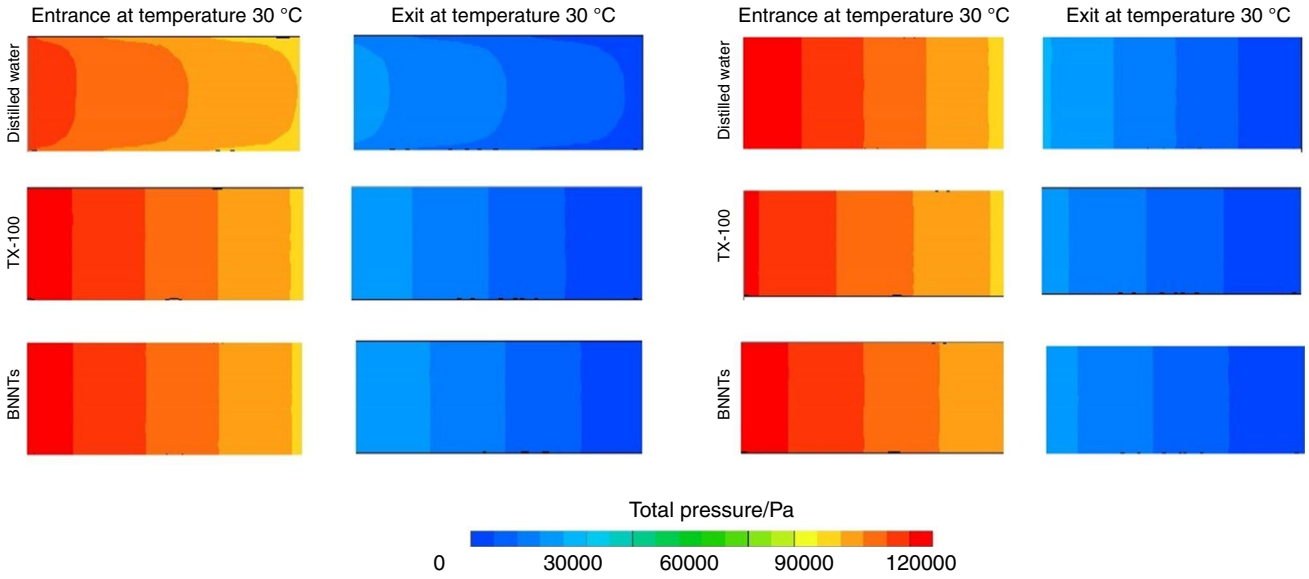

Fig. 3 Total pressure contour plot y-plane view ($y/w_c = 0.5$)

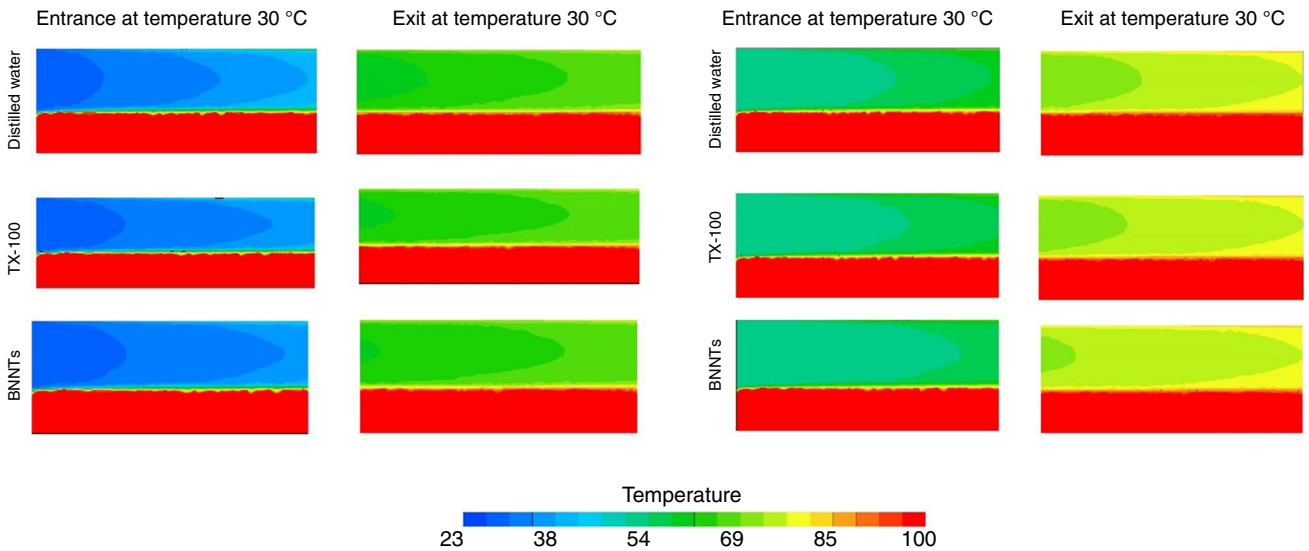

Fig. 4 Temperature contour plot y-plane view ($y/w_c = 0.5$)

and 0.9). The fluid flow pattern was observed in this view in which the gradual decrement in velocity from centre towards the wall, with a higher velocity observed at 50 °C. The total pressure appeared unsignificant pattern across the y-planed view as presented in one tone of colour legend, though the pressure is slightly higher halfway through the channel length for the fluids at 30 °C. For the temperature, as shown in Fig. 4, the fluids at 50 °C shown here is capable of absorbing more heat right from the entrance.

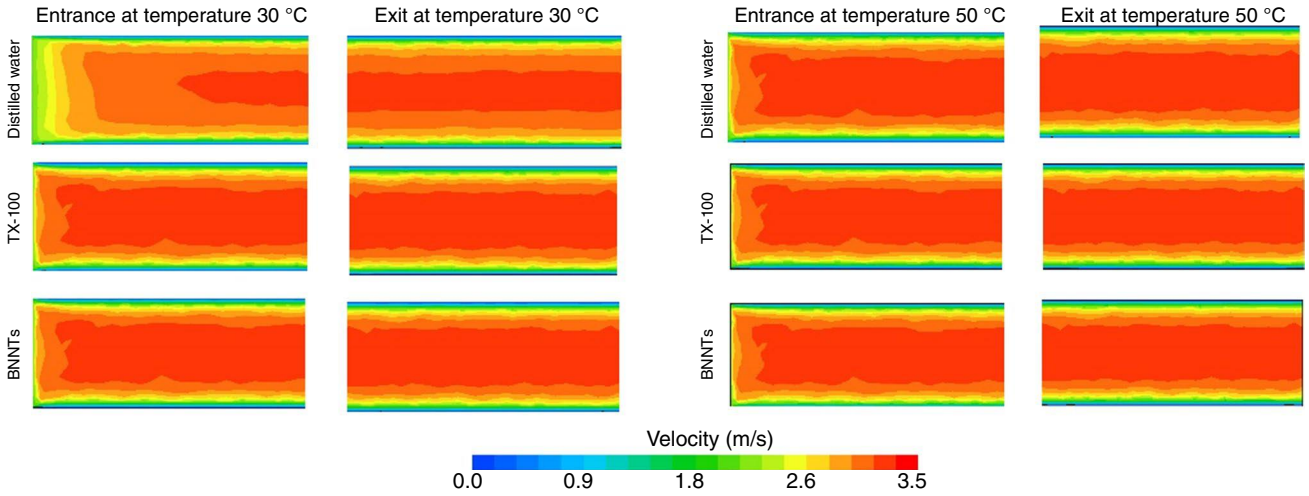

Fig. 5 Velocity contour plot y-plane view ($y/w_c = 0.5$)

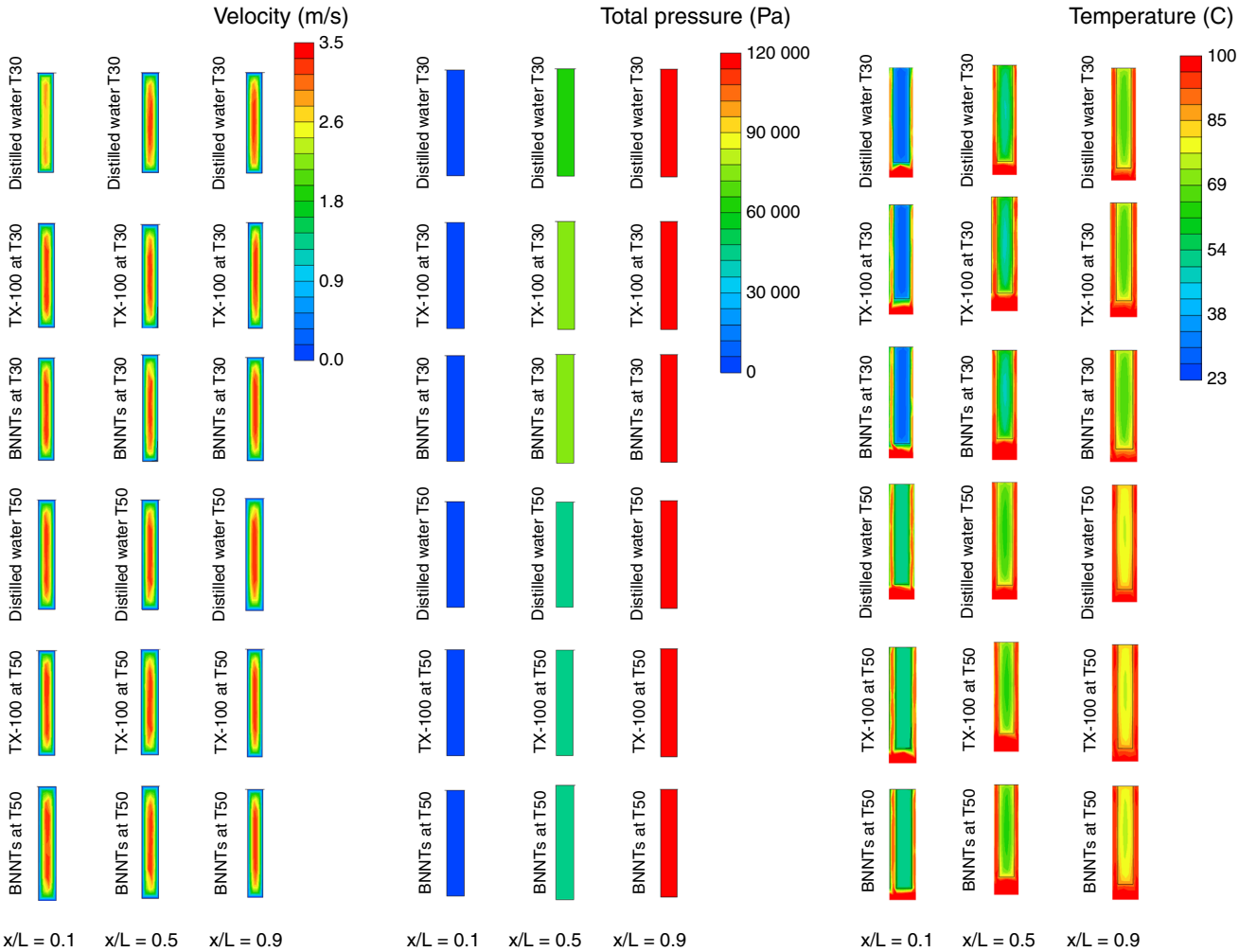

Fig. 6 Velocity, Total Pressure, and Temperature of plot y-plane view

Conclusion

In the present study, a CFD approach was adopted to investigate the flow characteristics and visualization of distilled water, TX-100 surfactant, and water, and BNNT nanofluid at two different temperatures, 30 and 50 °C respectively. Significant findings revealed that:

- Due to the lower density and much lower viscosity of the fluids at 50 °C, the *Re* for all fluids is about 60% higher than that at 30 °C.
- The Br number indicated that a higher heat transfer by viscous dissipation occurred for all fluids at 30 °C compared to that at 50 °C due much to the higher viscosity at that temperature.
- The pressure drops patterns observed at 30 °C agreed with a previous report on the significant effect of TX-100 surfactant on distilled water.
- As expected, the presence of the surfactant and BNNT in distilled water increased the frictional losses in the fluids investigated, and consequently, the pressure drops along the microchannel. However, the usage of TX-100 and BNNT to distilled water should be based on the objective of the application. If high heat flux removal become the priority than the pressure drops, thus this research data could provide reliable outcome of enhancing cooling capacity with minimal pressure drop.
- CFD modelling has shown the thermal and hydrodynamic developments along the microchannels investigated providing a better understanding of the trends and patterns that have been reported previously, in which the pressure and pumping power drop linearly across the channel and the Reynold number achieved stable fully developed flow after 0.2 relative length from the inlet flow.

Acknowledgements The authors would like to acknowledge Universiti Teknologi Malaysia (UTM) for providing CFD facility in conducting this research project.

References

1. Kamali R, Jalali Y, Binesh AR. Investigation of multiwall carbon nanotube-based nanofluid advantages in microchannel heat sinks. Micro Nano Letters. 2013;8(6):319–23.
2. Shamsuddin HS, Estellé P, Navas J, Mohd-Ghazali N, Mohamad M. Effects of surfactant and nanofluid on the performance and optimization of a microchannel heat sink. Int J Heat Mass Transf. 2021;175: 121336.
3. Ghorabaee H, Emami MRS, Shafahi M. Effect of nanofluid and surfactant on thermosyphon heat pipe performance. Heat Transfer Eng. 2020;41(21):1829–42.
4. Kiliç F, Menlik T, Sözen A. Effect of titanium dioxide/water nanofluid use on thermal performance of the flat plate solar collector. Sol Energy. 2018;164:101–8.
5. Li Y, Tung S, Schneider E, Xi S. A review on development of nanofluid preparation and characterization. Powder Technol. 2009;196(2):89–101.
6. Choi TJ, Jang SP, Kedzierski M. Effect of surfactants on the stability and solar thermal absorption characteristics of water-based nanofluids with multi-walled carbon nanotubes. Int J Heat Mass Transf. 2018;122:483–90.
7. Kameya Y, Hanamura K. Enhancement of solar radiation absorption using nanoparticle suspension. Sol Energy. 2011;85(2):299–307.
8. Suman S, Khan MK, Pathak M. Performance enhancement of solar collectors—A review. Renew Sustain Energy Rev. 2015;49:192–210.
9. Gómez-Villarejo R, Aguilar T, Hamze S, Estellé P, Navas J. Experimental analysis of water-based nanofluids using boron nitride nanotubes with improved thermal properties. J Mol Liq. 2019;277:93–103.
10. Taylor MA. Conservation of mass and energy for the moist atmospheric primitive equations on unstructured grids. In: Lauritzen Peter, Jablonowski Christiane, Taylor Mark, Nair Ramachandran, editors. Numerical techniques for global atmospheric models. UK: Springer; 2011. p. 357–80.
11. Hong F, Cheng P, Ge H, Joo GT. Conjugate heat transfer in fractal-shaped microchannel network heat sink for integrated microelectronic cooling application. Int J Heat Mass Transf. 2007;50(25–26):4986–98.
12. Halelfadl S, Adham AM, Mohd-Ghazali N, Maré T, Estellé P, Ahmad R. Optimization of thermal performances and pressure drop of rectangular microchannel heat sink using aqueous carbon nanotubes based nanofluid. Appl Therm Eng. 2014;62(2):492–9.
13. Tuckerman DB, Pease RFW. High-performance heat sinking for VLSI. IEEE Electron Device Lett. 1981;2(5):126–9.
14. Husain A, Kim K-Y. Optimization of a microchannel heat sink with temperature dependent fluid properties. Appl Therm Eng. 2008;28(8–9):1101–7.
15. Hosseinzadeh K, Roghani S, Mogharrebi A, Asadi A, Ganji D. Optimization of hybrid nanoparticles with mixture fluid flow in an octagonal porous medium by effect of radiation and magnetic field. J Therm Anal Calorim. 2021;143(2):1413–24.
16. Longest PW, Vinchurkar S. Effects of mesh style and grid convergence on particle deposition in bifurcating airway models with comparisons to experimental data. Med Eng Phys. 2007;29(3):350–66.
17. Habashi WG, Dompierre J, Bourgault Y, Ait-Ali-Yahia D, Fortin M, Vallet MG. Anisotropic mesh adaptation: Towards user-independent, mesh-independent and solver-independent CFD. Part I: General principles. Int J Numer Methods Fluids. 2000;32(6):725–44.
18. Bukar AL, Tan CW, Yiew LK, Ayop R, Tan W-S. A rule-based energy management scheme for long-term optimal capacity planning of grid-independent microgrid optimized by multi-objective grasshopper optimization algorithm. Energy Convers Manage. 2020;221: 113161.
19. Berni F, Cicalese G, Borghi M, Fontanesi S. Towards grid-independent 3D-CFD wall-function-based heat transfer models for complex industrial flows with focus on in-cylinder simulations. Appl Therm Eng. 2021;190: 116838.

Publisher's Note Springer Nature remains neutral with regard to jurisdictional claims in published maps and institutional affiliations.